The Astrophysical Journal, 923:163 (16pp), 2021 December 20 https://doi.org/10.3847/1538-4357/ac2e6d

Spatially Separated Electron and Proton Beams in a Simulated Solar Coronal Jet

Ross Pallister[1], Peter F. Wyper[2], David I. Pontin[1,3], C. Richard DeVore[4], and Federica Chiti[1]
[1] University of Dundee, School of Science and Engineering, Fulton Building, Dundee, DD1 4HN, UK; ross.pallister@northumbria.ac.uk
[2] Durham University, Department of Mathematical Sciences, Stockton Road, Durham, DH1 3LE, UK
[3] University of Newcastle, School of Mathematical and Physical Sciences, University Drive, Callaghan, NSW 2308, Australia
[4] NASA Goddard Space Flight Center, Heliophysics Science Division, Greenbelt Road, Greenbelt, MD 20771, USA
Received 2021 June 25; revised 2021 September 16; accepted 2021 October 9; published 2021 December 20

Abstract

Magnetic reconnection is widely accepted to be a major contributor to nonthermal particle acceleration in the solar atmosphere. In this paper we investigate particle acceleration during the impulsive phase of a coronal jet, which involves bursty reconnection at a magnetic null point. A test-particle approach is employed, using electromagnetic fields from a magnetohydrodynamic simulation of such a jet. Protons and electrons are found to be accelerated nonthermally both downwards toward the domain's lower boundary and the solar photosphere, and outwards along the axis of the coronal jet and into the heliosphere. A key finding is that a circular ribbon of particle deposition on the photosphere is predicted, with the protons and electrons concentrated in different parts of the ribbon. Furthermore, the outgoing protons and electrons form two spatially separated beams parallel to the axis of the jet, signatures that may be observable in in-situ observations of the heliosphere.

Unified Astronomy Thesaurus concepts: Active solar corona (1988); Solar flares (1496); Solar magnetic reconnection (1504); Solar magnetic bright points (1984); Solar electromagnetic emission (1490); Solar particle emission (1517)

1. Introduction

Explosive energy conversion occurs on a broad range of scales in the solar corona from nanoflares to large X-class flares. In these events, magnetic reconnection plays a critical role in rapidly converting stored magnetic energy into thermal and kinetic energy, as well as the energy associated with nonthermally accelerated particles. Among the ubiquitous phenomena observed on the Sun are coronal jets: collimated ejections of plasma launched by the impulsive onset of reconnection low in the solar atmosphere. Coronal jets are observed in multiple wavelengths and throughout the corona, including within coronal holes (Savcheva et al. 2007), in the quiet Sun (Panesar et al. 2016), and at the edges of active regions (Mulay et al. 2016), with differences in their typical properties in each region and at each wavelength. For example, based on a survey of jets observed in X-rays, Savcheva et al. (2007) found that coronal hole jets have typical lifetimes of around 10 minutes, bulk outflow velocities of around 200 km s^{-1}, and jet spire lengths and widths of around 50 Mm and 8 Mm, respectively. For further details of jets and their properties, see reviews by Raouafi et al. (2016) and Shen (2021).

The diffuse nature of the solar corona makes it extremely difficult to make direct observations of particle acceleration within reconnection regions. As such, we must rely on indirect observations from which aspects of the acceleration and reconnection processes can then be inferred. There are two principal ways that we can observe the high-energy particles accelerated by a coronal jet. First, if the jet is in an open magnetic field region (a coronal hole), then accelerated particles may stream directly out along open field lines. This provides the possibility to directly detect those particles in situ. Indeed, energetic helical jets on the edge of active regions, of the type recently simulated by Wyper et al. (2019), have been identified as the likely source of ^{3}He-rich impulsive solar energetic particles and energetic electrons measured in situ by the Solar Terrestrial Relations Observatory, the Advanced Composition Explorer, WIND, and the Parker Solar Probe (PSP; e.g., Krucker et al. 2011; Nitta et al. 2015; Innes et al. 2016; Bučík et al. 2018; Wiedenbeck et al. 2020). Whether less energetic coronal hole jets have identifiable in situ particle signatures is an open question.

Second, remote-sensing observations provide indirect evidence of particle acceleration in coronal jets. Type III radio bursts often occur in conjunction with energetic coronal hole jets observed at X-ray and extreme ultraviolet (EUV) wavelengths (e.g., Krucker et al. 2011; Nitta et al. 2015; Chen et al. 2018), suggesting that beams of energetic electrons are launched along open field lines by the jet reconnection (Krucker et al. 1999). Hard X-ray (HXR) coronal (Bain & Fletcher 2009; Glesener et al. 2012) and chromospheric (Glesener & Fleishman 2018; Musset et al. 2020) sources also indicate that nonthermal electron acceleration occurs within coronal jets. The positions and shapes of these sources relative to field structures have been used to diagnose the direction and location of the acceleration (e.g., Glesener et al. 2012). Finally, particles channeled downwards from the acceleration site toward the solar surface also give rise to flare ribbons that, depending upon the nature of the jet source region, can vary in complexity from a single bright point to multiple ribbons evolving throughout the event (e.g., Doyle et al. 2019; Kumar et al. 2019; Li & Yang 2019).

In this paper we examine nonthermal particle acceleration in a simulation of a coronal jet. As is common to essentially all coronal jets, the jet reconnection and particle acceleration occur within a dynamically evolving current sheet formed at a three-dimensional (3D) coronal null point. Our purpose is to

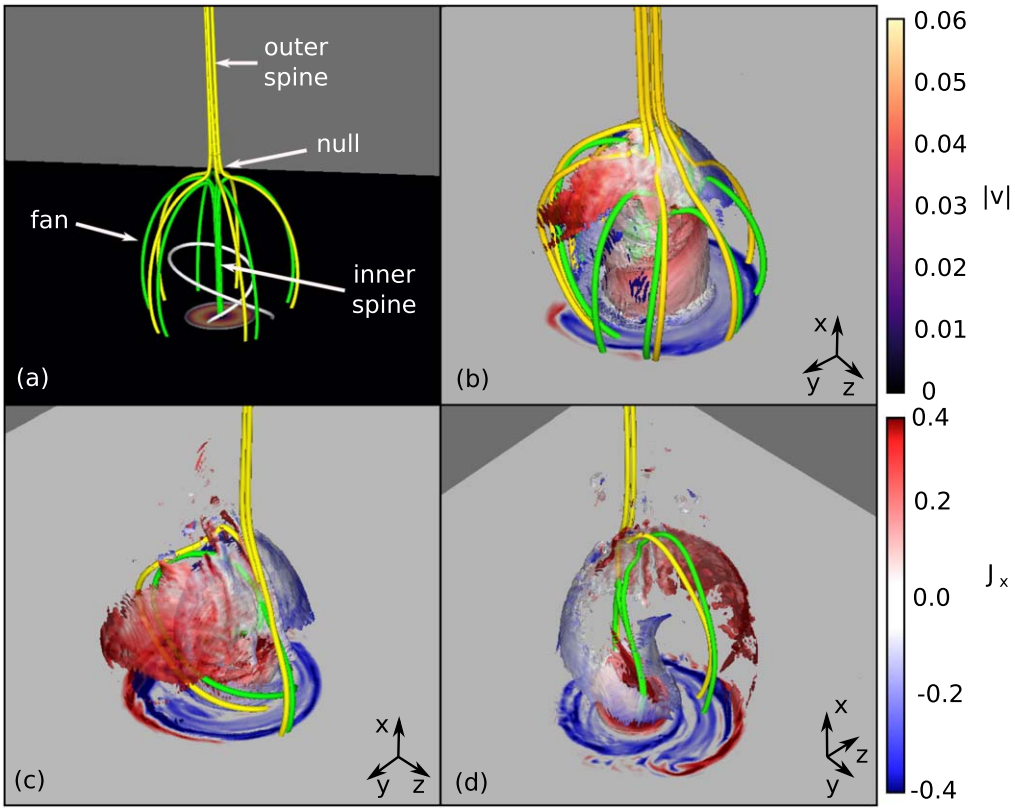

Figure 1. Evolution of the jet reconnection. (a) The pre-instability state at $t = 190$. Shading shows the surface driving and the gray contour shows the PIL. (b), (c), and (d) Evolution of the current layer during the jet at the three times studied ($t = 220$, 240, and 260 in nondimensional units, respectively). Semi-transparent isosurfaces show current density magnitude ((b): $J = 0.5$; (c) and (d): $J = 0.65$). In (b)–(d) color shading on the bottom boundary and on the isosurfaces indicates the vertical component of current (J_x).

determine the observable signatures of the nonthermal particles and to explore what can be learned from those signatures about the magnetic reconnection process driving the jet. We use the test-particle approach, whereby a large number of individual noninteracting charged particles are placed in electromagnetic fields derived from the simulation to produce spatial ejecta patterns and kinetic energy distributions (such as those discussed by Li et al. 2021). This test-particle approach has been widely used for probing particle acceleration in the corona. Stanier et al. (2012) modeled full particle motion to investigate nonthermal acceleration during spine and fan 3D null reconnection with static snapshots of the field geometries. Test-particle simulations have also been used to investigate charged particle motion in various magnetic field geometries in the solar system (e.g., Kress et al. 2007; Moore et al. 2010; Dalla et al. 2015, 2017; le Roux et al. 2015). To date, the majority of studies of particle acceleration during magnetic null-point reconnection have focused on the local vicinity of the null (Dalla & Browning 2005, 2008; Stanier et al. 2012; Pallister et al. 2019). Notable exceptions are the studies by Rosdahl & Galsgaard (2010) and Baumann et al. (2013), who found that particles were accelerated along the spine and fan structures associated with the null. In both studies, the current sheet at which the particles were accelerated is a single laminar structure. In this paper, we venture well beyond all of these previous results by modeling a jet in which the reconnection process is bursty, occurs in a fragmented region, and connects magnetically to remote parts of the solar atmosphere. These features are much more typical of an impulsively driven reconnection event in the corona (e.g., Ji & Daughton 2011).

Our jet simulation is similar to previous calculations (Pariat et al. 2009; Wyper & DeVore 2016; Wyper et al. 2016). The generic nature of the energy release process, which occurs in a fragmented dissipation region with a complex structure, is common to solar eruptive events more broadly, however. In the following Sections 2 and 3 we describe, respectively, the magnetohydrodynamic (MHD) simulation and the test-particle approach. In Section 4 we analyze the results of our particle simulations, and then in Section 5 we discuss their implications and present our conclusions.

2. MHD Simulation

We consider the scenario shown in Figure 1(a), whereby the minority polarity patch beneath a coronal null point is rotated by surface motions that add a twist to the closed field. The 3D null-point topology is defined by a separatrix surface (the fan plane), an inner spine that connects to the minority polarity on the solar surface, and an outer spine that extends into the open field and the heliosphere. Pariat et al. (2009) simulated a similar configuration and showed that, beyond the critical threshold of $N \approx 1.4$ turns, the twisted closed field becomes unstable to a kink-like instability whose onset breaks the symmetry of the system, induces explosive energy release via rapid null-point reconnection, and generates a helical jet. Recent observations suggest that most jets may involve the eruption of a small-scale filament channel from within the closed-field region (Sterling et al. 2015; Kumar et al. 2019). However, the explosive onset of intense null-point reconnection is a feature common to all jet

models and observations, so we expect the particle acceleration results derived from our simulation to be generic.

We adopt an initial nondimensionalized potential magnetic field of the form

$$\boldsymbol{B} = (-2, 0, 0) + \boldsymbol{\nabla} \times \boldsymbol{A}, \tag{1}$$

$$\boldsymbol{A} = \frac{bd^3}{2[(x - x_0)^2 + y^2 + z^2]^{3/2}}[-z\hat{\boldsymbol{y}} + y\hat{\boldsymbol{z}}], \tag{2}$$

with constants $b = 30$, $d = 1.5$, and $x_0 = -1.5$. The vertical direction in the Cartesian geometry is along the x coordinate, with the base positioned at $x = 0$. This setup is identical to that of Pariat et al. (2009), but with twice the field strength. A uniform plasma with $\rho = 1$ and $P = 10^{-2}$ is assumed, and gravity is neglected. The horizontal velocity imposed at the bottom boundary is given by

$$\boldsymbol{v}_\perp = v_0 g(B_x)\hat{\boldsymbol{x}} \times \boldsymbol{\nabla} B_x, \tag{3}$$

$$g(B_x) \equiv k_c \frac{B_r - B_l}{B_x} \tanh\left(k_c \frac{B_x - B_l}{B_r - B_l}\right), \tag{4}$$

in the region within which $B_l < B_x < B_r$, with constants $v_0 = 1.7 \times 10^{-4}$, $k_c = 5.0$, $B_r = 26$, and $B_l = 0.2$. Elsewhere, we set $\boldsymbol{v}_\perp = 0$, so that the entire bottom boundary is line tied. Figure 1(a) shows the driving ring created by this flow. To quasi-statically store twist in the closed field, the peak driving speed was chosen to be $v_{\max} \approx 0.055$, about 0.075% of the local Alfvén speed. The driving was smoothly ramped up from zero, held constant from $t = 50$ to $t = 190$, and then ramped down to zero at $t = 240$, once the kink instability was underway. A box size of $[x, y, z] \in [0{:}144, -18{:}18, -18{:}18]$ (in nondimensional units) was used with closed boundary conditions on the side (y and z) boundaries, and an open boundary condition at $x = 144$. To alleviate density depletion in the closed field during the driving, an open boundary condition was used at $x = 0$, whereby mass was allowed to flow into the domain from guard cells whose density and pressure were held fixed at their initial values throughout the simulation.

The nondimensionalized resistive MHD equations were solved with the Adaptively Refined Magnetohydrodynamics Solver (DeVore & Antiochos 2008) in the following form

$$\frac{\partial \rho}{\partial t} + \boldsymbol{\nabla} \cdot (\rho \boldsymbol{v}) = 0, \tag{5}$$

$$\frac{\partial (\rho \boldsymbol{v})}{\partial t} + \boldsymbol{\nabla} \cdot (\rho \boldsymbol{v}\boldsymbol{v}) + \boldsymbol{\nabla} P - \boldsymbol{J} \times \boldsymbol{B} = 0, \tag{6}$$

$$\frac{\partial U}{\partial t} + \boldsymbol{\nabla} \cdot (U\boldsymbol{v}) + P\boldsymbol{\nabla} \cdot \boldsymbol{v} = \eta J^2, \tag{7}$$

$$\frac{\partial \boldsymbol{B}}{\partial t} - \boldsymbol{\nabla} \times (\boldsymbol{v} \times \boldsymbol{B}) + \boldsymbol{\nabla} \times (\eta \boldsymbol{J}) = 0, \tag{8}$$

where t is the time, ρ is the mass density, $P = \rho RT$ is the thermal pressure, $U = P/(\Gamma - 1)$ is the internal energy density, $\boldsymbol{J} = \boldsymbol{\nabla} \times \boldsymbol{B}/\mu_0$ is the electric current density, $\mu_0 = 4\pi$ is the magnetic permeability, and $\boldsymbol{B}$ and $\boldsymbol{v}$ are the 3D magnetic and velocity fields. An ideal gas is assumed, with ratio of specific heats $\Gamma = 5/3$. The magnetic diffusivity η is given by

$$\eta = \begin{cases} \eta_0, & \mathcal{J} > \mathcal{J}_{\rm th} \\ \eta_0 \left(\dfrac{\mathcal{J}}{\mathcal{J}_{\rm th}}\right)^p, & \mathcal{J} < \mathcal{J}_{\rm th}, \end{cases} \tag{9}$$

where $\mathcal{J} = |\boldsymbol{J}|/|\boldsymbol{B}|$ with constants $\eta_0 = 16\pi \times 10^{-3}$, $\mathcal{J}_{\rm th} = 2.5$, and $p = 4$. This expression was chosen so that η was uniform within current sheets where nonideal effects dominate, $\mathcal{J} \gg \mathcal{J}_{\rm th}$, but decreased rapidly outside of the sheets, $\mathcal{J} < \mathcal{J}_{\rm th}$, to avoid diffusion of volumetric current in the twisted field region, i.e., depletion of the reservoir of free magnetic energy that powers the jet. With these parameter choices the current layer that forms at the null during the jet resides nearly entirely within the locally uniform resistivity region. To further avoid diffusion of the twisted field, η was set to zero for $t < 190$, switching on just prior to the onset of the kink instability ($t \approx 200$). Prior to the onset of the kink instability, reconnection at the null point is inhibited by the cylindrical symmetry of the system (Pariat et al. 2009; Rachmeler et al. 2010).

A rectangular region of maximal grid refinement large enough to encompass the separatrix and the early evolution of the jet was used. Within this region the grid is uniform with a grid spacing of $\Delta \approx 4.7 \times 10^{-2}$. Outside of this region, the background grid resolution was lower and the grid adapted dynamically with time as the current structures developed, following Karpen et al. (2012).

To scale the nondimensional simulation results to typical coronal hole jet values the following scaling factors were applied: $l_0 = 2.5$ Mm (for all nondimensional lengths), $B_0 = 10^{-4}$ T (so the electric field scales as $E_0 = 10$ V m^{-1}) and $\rho_0 = 4.8 \times 10^{-14}$ kg m^{-3}. Correspondingly, units of simulation time are scaled by $t_0 \approx 1.9$ s, the ambient plasma temperature becomes $T \approx 1.0$ MK, the width of the separatrix dome becomes $w \approx 17$ Mm, and vertical outflow velocities within the jet reach several hundred km s^{-1}.

The jet begins around $t = 6$ minutes 30 s into the simulation and has a duration of about 6 minutes. Figures 1(b) to (d) shows the current sheet evolution at the three time frames we have chosen for further study. The first at $t = 220$ (7 minutes 6 s) corresponds to shortly after the onset of the kink. The current layer is relatively smooth at this point. The second at $t = 240$ (7 minutes 45 s) is further into the evolution of the kink, which is in the process of broadening and lengthening the current layer. The final snapshot at $t = 260$ (8 minutes 24 s) is during the most intense phase of reconnection once the jet is well underway. At this time, the current sheet has evolved into a broad helical shape and contains multiple tearing-induced null points and small-scale flux ropes.[5] To study how particles would be accelerated within the current layer during the jet, snapshots of the magnetic and electric fields at each of these times were taken as inputs to the test-particle code.

3. Test-particle Methods

3.1. Equations of Motion

The trajectories of particles in the domain were calculated using a variable time step test-particle code. The equations of

[5] We identify the null points using the trilinear method described by Haynes & Parnell (2007), using an implementation by Chiti (2020) that can be found at https://zenodo.org/record/4308622#.YCXany2w0wc.

charged particle motion in the presence of electric and magnetic fields are solved, neglecting gravitational forces and particle−particle interactions. The full motion of charged particles is described by equations of motion derived from the relativistic Lorentz force,

$$\frac{d\boldsymbol{p}}{dt} = q\left(\boldsymbol{E}(\boldsymbol{r}) + \frac{\boldsymbol{p}}{\gamma m_0} \times \boldsymbol{B}(\boldsymbol{r})\right), \tag{10}$$

$$\frac{d\boldsymbol{r}}{dt} = \frac{\boldsymbol{p}}{m_0 \gamma}, \tag{11}$$

$$\gamma = \frac{1}{\sqrt{1 - \frac{v^2}{c^2}}}, \tag{12}$$

where $\boldsymbol{p}$ is the particle momentum, $\boldsymbol{r}$ is the particle Cartesian position, γ is the Lorentz factor, m_0 is the rest mass, and $v = |d\boldsymbol{r}/dt|$ is the speed. The field values $\boldsymbol{B}$ and $\boldsymbol{E}$ at particle position $\boldsymbol{r}$ are determined using a trilinear interpolation of values on the MHD simulation grid. The electric field values $\boldsymbol{E}$ are not generated directly by the MHD simulation, but rather are calculated at each grid point using the resistive Ohm's law,

$$\boldsymbol{E} = -\boldsymbol{v} \times \boldsymbol{B} + \eta \boldsymbol{J}. \tag{13}$$

Following the full orbits of electrons, in particular, can become prohibitively computationally expensive. Therefore, our test-particle code switches dynamically between modeling the full motion of a particle according to the relativistic Lorentz force above and the guiding-center approximation in which a particle is assumed to gyrate around a magnetic field line. The equations of motion in the guiding-center approximation are as follows (e.g., Northrop 1961, 1963):

$$\frac{dU_{\parallel}}{dt} = \frac{d(\gamma v_{\parallel})}{dt} = \gamma \boldsymbol{U}_E \cdot \frac{d\hat{\boldsymbol{B}}}{dt} + \Omega_{\rm scl} t_{\rm scl} E_{\parallel} - \frac{\mu_r}{\gamma}\frac{\partial B}{\partial r}, \tag{14}$$

$$\frac{d\boldsymbol{R}_{\perp}}{dt} = \boldsymbol{U}_E + \frac{\hat{\boldsymbol{B}}}{B^{**}} \times \left\{ \frac{1}{\Omega_{\rm scl} t_{\rm scl}} \left[\frac{\mu_r}{\gamma} \left(\nabla B^* + \frac{v_{\rm scl}^2}{c^2} \boldsymbol{U}_E \frac{\partial B^*}{\partial t} \right) + U_{\parallel} \frac{d\hat{\boldsymbol{B}}}{dt} + \gamma \frac{\boldsymbol{U}_E}{dt} \right] + \frac{v_{\rm scl}^2}{c^2} \frac{\mu_r}{\gamma} E_{\parallel} \boldsymbol{U}_E \right\}, \tag{15}$$

$$\frac{d\gamma}{dt} = \frac{v_{\rm scl}^2}{c^2} \left[\Omega_{\rm scl} t_{\rm scl} \left(\frac{d\boldsymbol{R}_{\perp}}{dt} + \frac{U_{\parallel}}{\gamma} \hat{\boldsymbol{B}} \right) \cdot \boldsymbol{E} + \frac{\mu_r}{\gamma} \frac{\partial B^*}{\partial t} \right], \tag{16}$$

$$\mu_r = \frac{\gamma^2 v_{\perp}^2}{B}, \tag{17}$$

$$B^* \equiv B\left(1 - \frac{1}{c^2}\frac{E_{\perp}^2}{B^2}\right)^{\frac{1}{2}}, \tag{18}$$

$$B^{**} \equiv B\left(1 - \frac{1}{c^2}\frac{E_{\perp}^2}{B^2}\right). \tag{19}$$

$\boldsymbol{E}$ and $\boldsymbol{B}$ are the electric and magnetic fields, respectively, with $\hat{\boldsymbol{B}}$ as the unit vector of $\boldsymbol{B}$. Velocity term $v_{||}$ is the velocity component parallel to $\boldsymbol{B}$ and $\boldsymbol{U}_E$ is the velocity component due to $\boldsymbol{E} \times \boldsymbol{B}$ particle drift. Terms $v_{\rm scl}$, $t_{\rm scl}$, and $\Omega_{\rm scl}$ are the scaling factors for velocity, time, and gyrofrequency, respectively, and μ_r is the magnetic moment, which is taken to be conserved throughout the guiding-center integration. $\boldsymbol{R}$ is the gyrocenter of the particle, so that $\frac{d\boldsymbol{R}_{\perp}}{dt}$ is the velocity of the particle perpendicular to $\boldsymbol{B}$, with magnitude $v_{\perp}$.

As the exact position of the particle is unknown in the guiding-center approximation, its position vector cannot be used to interpolate the field values in the local grid cell. For this purpose it is assumed that the field values are approximately equal across the orbit, so the field is instead evaluated using the location of the guiding-center position.

We assume the electromagnetic fields to be static on the timescale of particle integration, so that time derivatives of $\boldsymbol{B}$ in Equations (14)–(16) are neglected. The protons and electrons were simulated for 10 and 3 s respectively, compared to the Alfvén travel time across the dome of the jet, approximately 3.5 s. While the electron run time satisfies the assumption by being shorter than this travel time, the assumption for the protons is less well supported, though such a long run time was necessary to produce good proton ejecta statistics. Values for the spatial derivatives of $\boldsymbol{B}$ and $\boldsymbol{E}$ at any value of $\boldsymbol{r}$ are, however, required. Where the input grid data do not include these values (as is typical for MHD simulations) they must first be approximated for each vertex of a local cell prior to trilinear interpolation. This was done using a central difference method.

The full-motion Equations (10) are solved using a sixth-order Adams predictor-corrector scheme, while the guiding-center Equations (14)–(16) are solved with a fourth-order Runge–Kutta method adapted from the well-established and thoroughly tested `party_orb` code[6] (see Wood & Neukirch 2005; Grady et al. 2012; Threlfall et al. 2015, 2016; Borissov et al. 2017, for details and prior applications of this code).

The particles are initialized in the full-motion scheme. The code switches to using the guiding-center equations when the conditions for validity of this approximation are satisfied. First, the magnetic field gradient must be negligible across the particle orbit; second, the electric field component parallel to the magnetic field vector must be significantly smaller than the perpendicular component. If either of these conditions is not satisfied or if the particle approaches the boundary of the domain, the code switches back to full-motion. Details of how the switching is performed are presented in Appendix C.

There are limitations to the current test-particle implementation that, while common to prior test-particle simulation work, should nonetheless be borne in mind when interpreting results produced by this method. How the following effects would influence our results, were they included, is discussed in Section 5. The primary limitation of the test-particle approach is the lack of self-consistency between the particles and the magnetic and electric fields. Beams of accelerated particles constitute a current, with an associated induced magnetic field. If only a small number of particles is accelerated in the system under study, this does not pose a major problem, since the induced field would be small compared to the field obtained via the MHD simulation. However, if the number of accelerated particles is large this is not the case and self-consistency is lost. In addition, charge separation caused by acceleration of protons and electrons in opposite directions should set up an electric field, which is again absent from the MHD description.

Direct particle−particle interactions such as scattering are neglected, where realistically a particle would undergo multiple scattering events over the length of the domain. Scattering has

[6] Available at https://github.com/jwt104/party_orb.

two main effects: first, high-energy particles are decelerated when scattered via lower-energy particles. As such, one would expect higher kinetic energies in simulations where particles are accelerated uninterrupted. The second effect is the change in direction and subsequent change in pitch angle of the scattered particle. Particles that do not undergo scattering are more strongly aligned to local field lines and the pitch-angle distribution would not undergo the expected diffusion.

With these caveats in mind, the test-particle approach using MHD simulations has nevertheless been extensively used and provides a useful method to probe the trajectories of accelerated particles in large systems such as the one considered here.

3.2. Test-particle Initialization

We initialize and follow the motions of a total of 5×10^4 particles: 2.5×10^4 protons and 2.5×10^4 electrons. This is a very small fraction of the total number of particles in the equivalent volume in the base MHD simulations (of order 10^{33} particles for a seeded number density of 5.7×10^7 cm^{-3}), and is intended only to demonstrate a representative set of accelerated particle trajectories.

In the vast majority of the domain we expect negligible particle acceleration on the timescale of our particle simulations. Therefore, for computational efficiency we preferentially initialize particles in locations where acceleration is most likely. We do this by initializing particles within regions of large current density $|\boldsymbol{J}|$ relative to $|\boldsymbol{B}|$. This is achieved as follows. Particles were given a random initial position within the reduced domain $x \in [0,\ 70l_0]$, $y \in [-15l_0,\ 15l_0]$, and $z \in [-15l_0, 15l_0]$, as this covers the regions where the current structures are found. The value of $|J|/|B|$ at that position was then calculated and compared to a user-selected threshold value. If $|J|/|B|$ exceeded this value, the position was accepted. Otherwise, the position was rejected and the process was repeated with a new random position. The threshold value was selected to ensure that particles would not be initialized far from the regions of relatively high current density. This value was chosen to be $|J|/|B| = 1 \times 10^{-2}$ in dimensionless units from the MHD simulation.

The particles are assumed to have initially thermal energies. Their initial momenta are randomized as a Maxwellian distribution based on the temperature scaling factor, $T_0 = 10^6$ K (where the nondimensional temperature is 1). On examination, we find that the bulk velocities in the inflow regions of the MHD simulation were negligible compared to these thermal velocities. Hence, the bulk flow was neglected when initializing the particle velocities. Protons and electrons were simulated for 10 s and 3 s, respectively.

4. Test-particle Results and Discussion

4.1. High-energy Trajectories

During our particle simulations, both protons and electrons are found to be accelerated down toward the photosphere ($x = 0$) and also outwards toward the heliosphere ($x \gg 1$). In order to better understand how this acceleration occurs, and to reveal what the spatial particle distribution tells us, we compare the patterns of acceleration with the magnetic field "skeleton." In particular, we use the trilinear method outlined by Haynes & Parnell (2007) and implemented by Chiti (2020) to find the magnetic null points within the domain, and then plot sample field lines passing close to these nulls. We also evaluate the magnetic squashing factor, Q (Titov et al. 2004), between the lower and upper domain boundaries. This quantity reveals regions where the field-line mapping becomes highly distorted. In addition, we record whether field lines are closed (both ends connect to the plane $x = 0$) or open (one end connects to each of the planes $x = 0$ and $x = 90l_0$).

Figure 2 shows the trajectories of the 250 most energetic particles (top 1%) in each snapshot, for protons and electrons separately. The trajectories are plotted together with magnetic null-adjacent field lines (NAFLs). For NAFLs we plot field lines seeded at the approximate null-point location and at the vertices of a cube centered on the null point with side length 4×10^{-2} (10^5 m). We find three nulls at $t = 220$, one at $t = 240$, and 11 at $t = 260$. A larger number of magnetic null points indicates a more complicated field geometry, which is expected to guide particles in more elaborate trajectories.

Examining the top row of Figure 2, certain features are broadly apparent. First, the majority of the NAFLs impact the photosphere on the boundary between open and closed flux. This is expected since many of these field lines will closely follow the fan separatrix surface of the null(s). A single blue curve connects down into the center of the closed-field region on the photosphere. This is the analog of the "closed spine" of the null in the initial condition (at this time the three nulls are only separated by about $1.5l_0$), so the large-scale topology is very similar to the case with a single null. Second, we observe that the majority of high-energy particle trajectories also connect down to the photosphere, impacting along the boundary between open and closed flux. This is a strong indication that, as expected, the particles are being accelerated in the vicinity of the nulls and are guided along the field lines adjacent to those nulls (e.g., Rosdahl & Galsgaard 2010; Baumann et al. 2013; Pallister et al. 2019). The magnetic reconnection that is induced is the spine-fan mode, which permits flux transport across the separatrix surface: in this mode of reconnection the electric field is parallel to the separatrix (fan) surface (Pontin et al. 2007; Priest & Pontin 2009), so the majority of particles adhere to the fan. A portion of this population is accelerated toward the null and is deflected along the open and closed spine lines (see Section 4.4 and Figure 7).

At the $t = 240$ and $t = 260$ snapshots, the dome separatrix structure has become substantially distorted as the jet progresses. By $t = 260$, a current-layer instability has occurred such that 11 nulls are now present (Wyper & Pontin 2014a; Wyper et al. 2016) and their NAFLs start to intertwine. While the NAFLs and high-energy particle trajectories continue to adhere closely to the magnetic field connectivity boundaries, they are substantially more complex due to the increase in topological complexity (see Section 2). High-energy particles are accelerated both down toward the photospheric boundary and outwards along the jet into the heliosphere. We examine the possible observational signatures of these two populations in turn.

4.2. Photosphere Impact Maps

The particles accelerated downwards will impact the denser plasma of the chromosphere and photosphere, leading to emissions across a range of wavelengths (e.g., Zharkova et al. 2011, and references therein). We find significant differences in the trajectories and impact positions of high-energy protons and electrons for all snapshots. Figure 3 shows the photospheric impact maps of the incident protons and electrons at each time, overlaid on the Q map at the photospheric boundary (note that Q is modified with a masking function such that negative

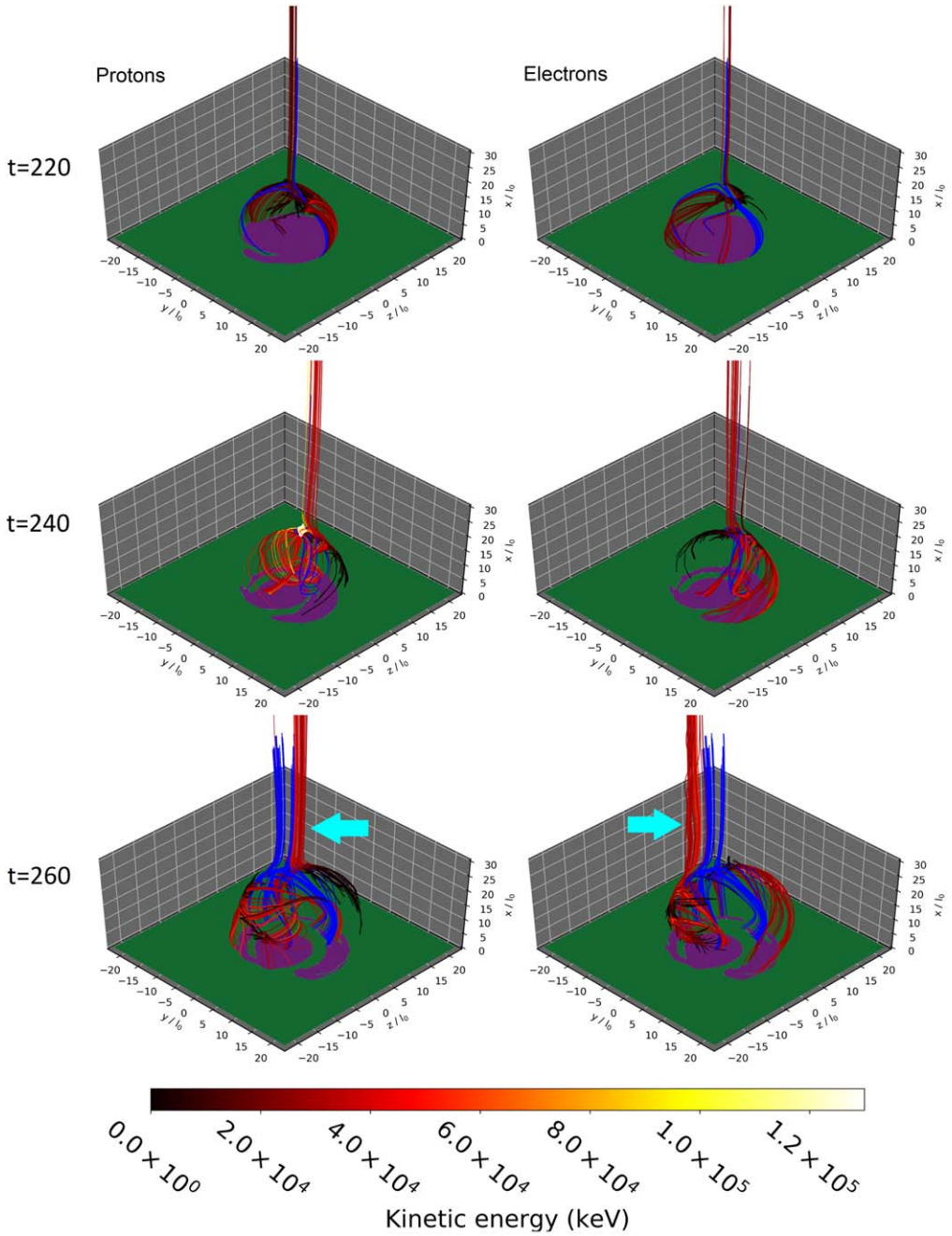

Figure 2. Trajectories of the 250 protons (left) and 250 electrons (right) with highest final kinetic energies (top 1%) at $t = 220$, 240, and 260, color coded according to kinetic energy. Blue lines are field lines seeded adjacent to the magnetic null points (nine field lines per null point). At $x = 0.0$ are binary contour plots where green represents open-field regions and purple represents closed-field regions. Cyan arrows highlight the particle beams at $t = 260$.

values denote closed field and positive values open field—see Appendix D for details). Blue circles on the Q maps show the impact positions of the NAFLs. Concave features on the Q maps where two sections of the open/closed boundary are close together are associated with flux-rope field lines, which are formed during tearing of the current sheet (Wyper & Pontin 2014b; Wyper et al. 2016).

Examining the separate impact patterns of protons and electrons along the boundary between open and closed flux, we see that they tend to fill in roughly complementary parts of that boundary. This tendency results from the opposite electric charges of protons and electrons, coupled with the (broadly) unidirectional electric field within the current layer: protons are accelerated one way along this potential drop, and electrons the other. While not modeled in the test-particle method, this separation of charges would realistically result in the formation of an electric field where this occurs, further accelerating subsequent particles that are directed into this region. Such an effect could be modeled with a kinetic simulation.

Inspecting the open/closed boundary in more detail, we find high-energy particles impacting the photosphere at concave features at the boundary of the Q map, such as those at (y, z) $\approx (-9,\ 0)\ l_0$ at $t = 220$ and at (y, z) $\approx (0,\ 9)\ l_0$ and (y, z) $\approx (12,\ 0)\ l_0$ at $t = 260$. This suggests that field structures that connect to the photosphere at these features, such as flux ropes, are also guiding high-energy protons and electrons.

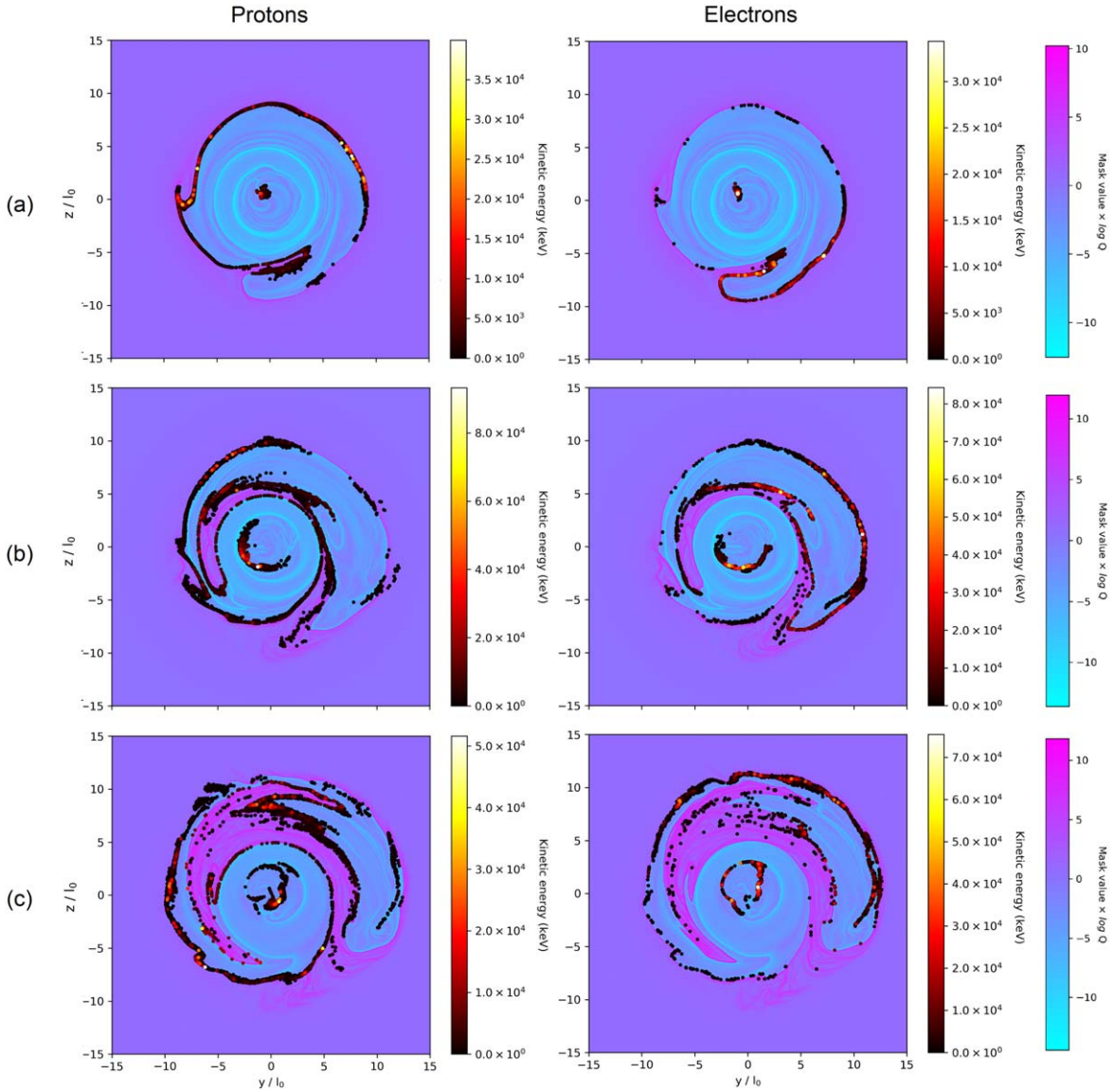

Figure 3. Contour plots of masked log squashing factor Q (see Appendix D) overlaid with proton and electron impact positions and kinetic energies at $x = +0.01$, close to the photospheric boundary, for (a) $t = 220$, (b) $t = 240$, and (c) $t = 260$.

Both protons and electrons are accelerated along the spine axis, outwards parallel to the outer spine and downwards toward the photospheric footpoint of the inner spine. At $t = 220$, the latter forms a relatively compact impact site close to $(y, z) = (0, 0)$. However, as the coronal null point becomes more distorted ($t = 240$) and eventually breaks up into multiple nulls ($t = 260$), the trajectories around the spine that pass close to the null are stretched out into a ribbon along which the squashing factor Q is high (Masson et al. 2009; Pontin et al. 2016; Masson et al. 2017). High-energy protons and electrons impact the photosphere at different locations in y and z along this ribbon, a point to which we will return later.

4.3. Binned Energy-deposition Maps

The impact maps of individual particles tell us where high-energy particles are being absorbed. For comparison with observed emissions created when particles impact the chromosphere and photosphere, however, a map of the total energy crossing the photospheric boundary across bins of a fixed size is more useful. Figure 4 shows particle impact maps on the photosphere in which we have summed the energies of all particles that impact within a prescribed spatial bin. They are displayed in two resolutions, 45×45 and 300×300, corresponding to bins of length 833 km and 125 km, respectively. These spatial resolutions approximate those of the Solar Dynamics Observatory's Atmospheric Imaging Assembly (Lemen et al. 2012) and the Interface Region Imaging Spectrograph (De Pontieu et al. 2014), respectively, for our choice of l_0.

There are some caveats that should be borne in mind when interpreting these binned energy-deposition maps in the context of predicted luminosity. First, the total energy in the bins scales with the number of particles integrated, so what is physically relevant is the relative differences between the plots rather than the absolute values for any one plot. Second, the plots show the cumulative energy of all particles crossing the photospheric boundary $x = 0$ during each snapshot. To equate these maps to luminosity maps, we assume that effectively all of the incident energy is emitted; no proper target model has been used. In

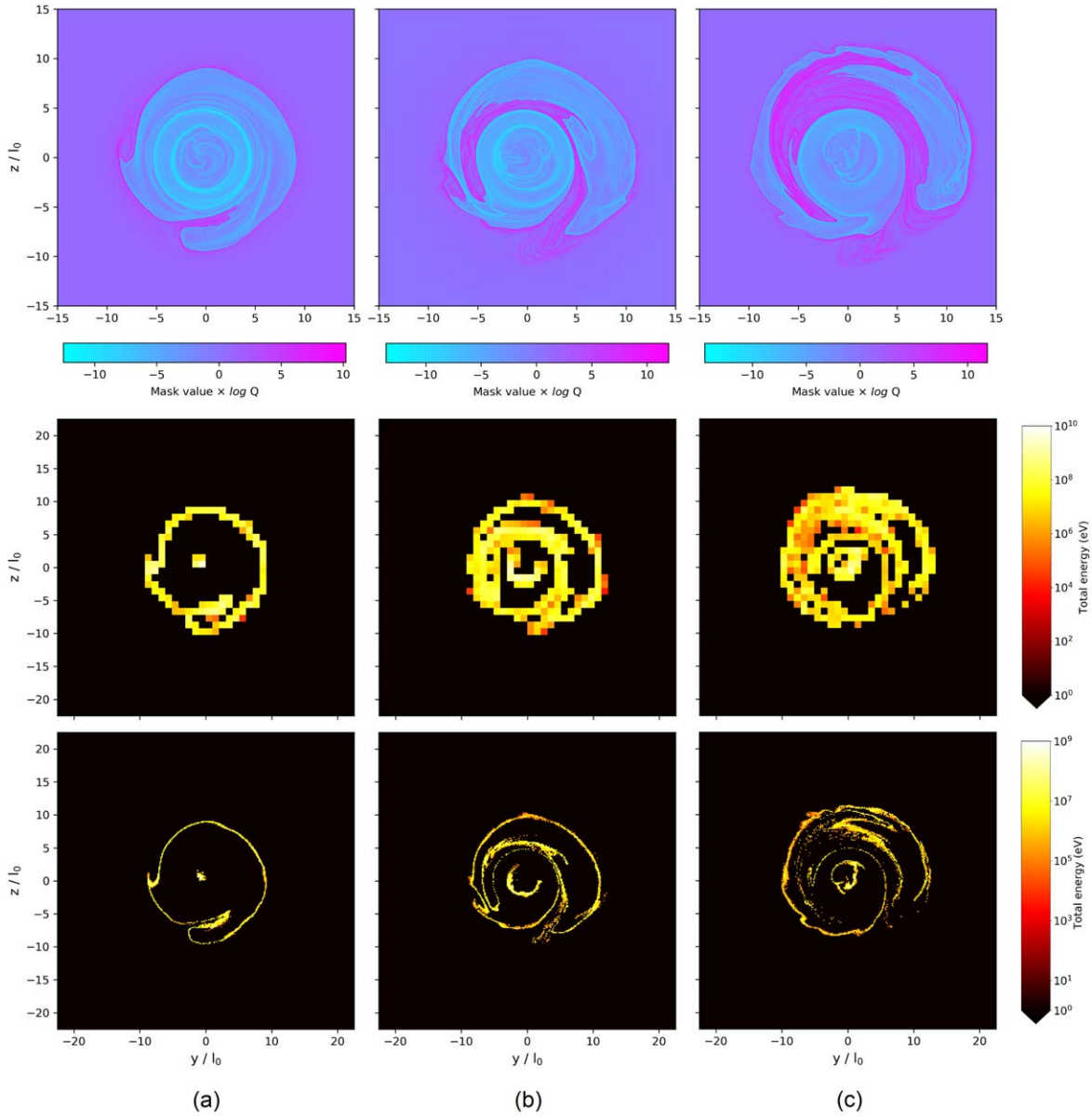

Figure 4. Binned energy-deposition maps on the photosphere, for two different resolutions, where $l_0 = 2.5$ Mm: (a) $t = 220$, (b) $t = 240$, and (c) $t = 260$. Top row: contour plots of masked log squashing factor Q. Middle row: cumulative energy of particles incident on the photospheric boundary at $x = +0.01$ with resolution 45×45. Bottom row: cumulative energy of particles incident on the photospheric boundary at $x = +0.01$ with resolution 300×300.

addition, penetration of the photosphere is not considered, so it is assumed that all particles are decelerated there. Second, as these are cumulative energy maps, there is no distinction between emitted wavelengths from particles of different energies. Instead, we treat them as luminosity plots integrated over all wavelengths. What we can compare with flare luminosity features is the shape and evolution of the maps over time. These features include flare ribbons and HXR footpoints that are observed on the photosphere during coronal jets.

At both resolutions, the bins that trace the Q map boundary are those that have high energies, whereas the highest total energies are located at the central spine impact positions. There are numerous features around the circular ribbon that appear substantially brighter than at other points; these may correspond to the observed bright knots or kernels within flare ribbons. The concave features that form at the footpoints of flux ropes appear, if anything, to correspond to lower energies. However, the ribbon also tends to be broader at those locations, so the lower total energy in the bins probably comes mostly from a spreading of the energy perpendicular to the ribbon, rather than a lower total energy along the ribbon at that location. Our results closely resemble the quasi-circular EUV emission, accompanied by a central bright point, observed in many on-disk coronal jets (e.g., Panesar et al. 2016; Kumar et al. 2019). Our results also provide a possible explanation for some of the dynamic substructure within the observed features.

4.4. Heliospheric Ejection Maps

We now examine the patterns of accelerated particles crossing large heights $x = 60$ (150 Mm) in the simulation domain, in order to understand expected particle signatures of in situ measurements by, for example, the PSP. Figures 5 and 6 show the crossing positions of protons and electrons on the

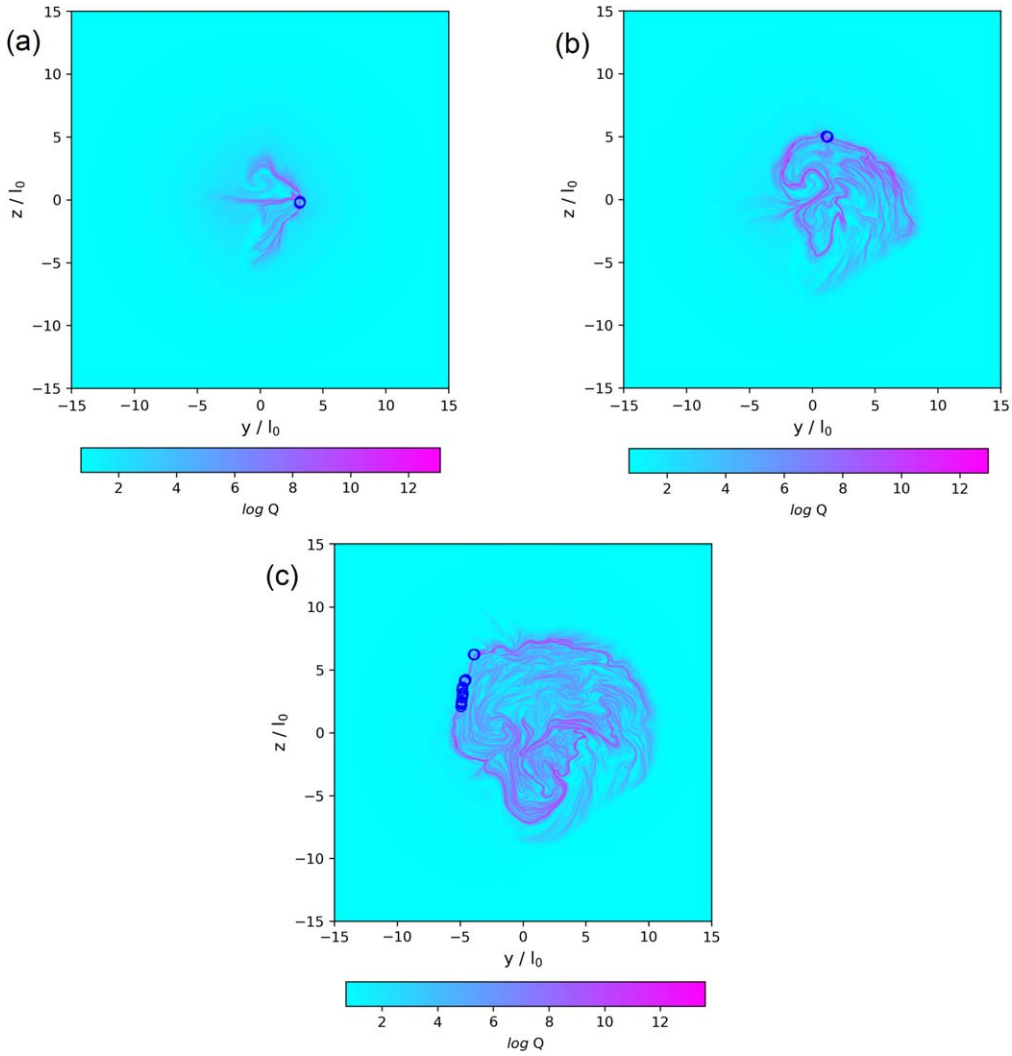

Figure 5. Contour plots of log squashing factor Q overlaid with null-adjacent field-line crossing positions (blue circles) at $x = +60.0$, cut across the jet entering the heliosphere, for (a) $t = 220$, (b) $t = 240$, and (c) $t = 260$. Please note that the log Q map color scaling has changed from Figures 3 and 4, as the log Q values are no longer masked.

plane $x = 60$, overlaid on the Q distribution. At this plane, the field lines of the jet are approximately aligned to the $+x$-direction and the plane is sufficiently far from the evolving dome structure that these particles are no longer accelerating. The NAFLs that cross this boundary are also displayed.

Regarding the magnetic field topology, we note that the position at which the spine field line(s) intersect(s) this plane rotate(s) around the jet axis (roughly around $(y, z) = (0, 0)$) in a counterclockwise sense, as the dome evolves. The intersection of the spine(s) lie(s) along a ridge of high Q that lengthens and becomes more pronounced throughout the jet. This ridge marks the boundary between the smooth pre-reconnection open field and the highly structured post-reconnection field lines within the jet. As explained in Wyper et al. (2016) for the case of closed-field jets, this highly structured region of Q results from turbulence and mismatched flux-tube lengths within the jet. The region grows in area as the jet develops and more open field lines reconnect.

Incident protons and electrons of all energies are found to be closely aligned with these high-Q ridges. At $t = 220$ and $t = 240$, the highest-energy protons cross the plane close to, but slightly clockwise of, the positions of the field lines. At $t = 260$, multiple nulls are present (see above), so that the NAFLs outline the location of open spines and field lines from "separatrix curtains" bounded by these spines (Titov et al. 2011; Platten et al. 2014). In this case, the highest-energy protons also breach the plane along the Q ridge extending clockwise from the lowest (in z) position. However, they now also extend between the other clusters of NAFL positions, likely as a result of the extra topological structure.

Examining now the crossing distributions of electrons (right-hand column of Figure 6), we see that, at $t = 220$ and $t = 240$, the high-energy electrons also cross close to the positions of the spines but now along the section of the Q ridge that extends *counterclockwise* from the NAFL positions. This can also be seen at $t = 260$, where the majority of the high-energy electrons lie along the ridge of high Q extending counterclockwise of the lowest (in z) position. Compared to the protons, many fewer high-energy electrons end up between the clusters.

Our interpretation of the behavior that leads to this dichotomy between the electron and proton crossing positions is as follows. Consider a particle initiated at a location in the current sheet as marked by the orange/yellow circles in Figure 7. Depending upon the sign of the particle's charge, it

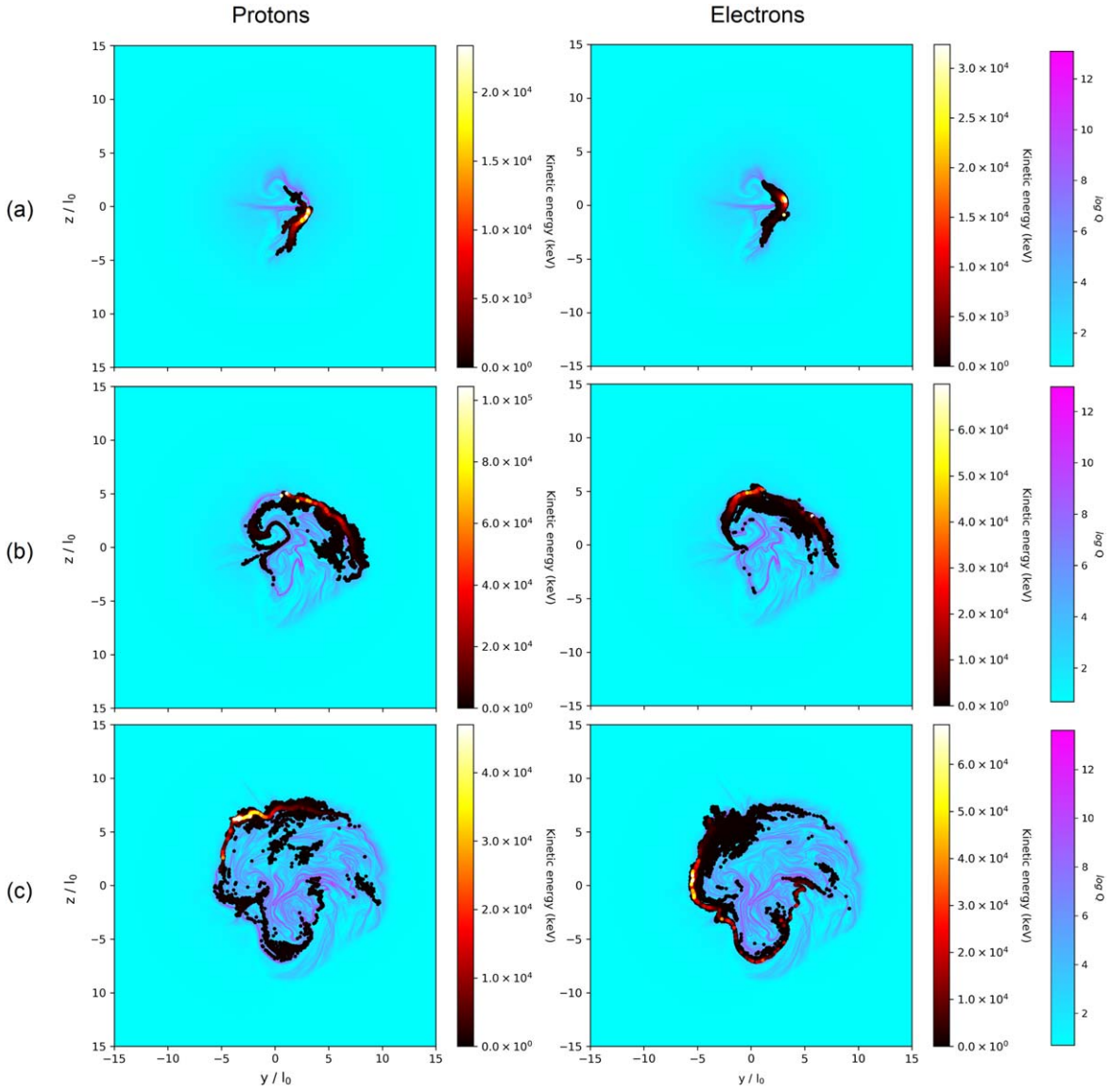

Figure 6. Contour plots of log squashing factor Q overlaid with proton and electron crossing positions and kinetic energies at $x = +60.0$, cut across the jet entering the heliosphere, for (a) $t = 220$, (b) $t = 240$, and (c) $t = 260$.

will be accelerated either toward or away from the null. Particles accelerated toward the null will tend to be guided along the field lines either up or down the spine. The field geometry is such that, so long as the null is not exactly rotationally symmetric, the field lines passing close to the null tend to stretch out to form an extended ribbon or ridge, as explained by Pontin et al. (2016) and indicated by the contours of Q on the lower/upper boundaries.[7] Therefore, the two halves of this high-Q ribbon/ridge are expected to be sites for the arrival of oppositely charged particle beams, with the spine footpoint between the two. These distinct beams are visible in the particle trajectories shown in Figure 2, most notably at $t = 260$. While the local field geometry and the particle paths in the weak-field region of our simulation are substantially complicated by the formation of additional nulls, on average the above arguments are expected to hold.

[7] These contours are taken from a linear null in a cubic domain based on the calculations of Pontin et al. (2016), but the qualitative shape is not affected by the dome geometry.

The key result is that high-energy protons and electrons are accelerated in two separated beams, both in the presence of a single null ($t = 220$, 240) and a null cluster ($t = 260$). This clear separation between protons and electrons ejected adjacent to the outer spine could result in an observable in situ signal of distinct proton and electron beams.

4.5. Total Accelerated Populations and Energy Distributions

Table 1 enumerates the fraction of particles that cross either the photospheric ($0.01 l_0$) or heliospheric ($+60.0 l_0$) boundary. This fraction is expressed by the percentage of total particles of *all* species, i.e., up to a maximum of 50% for either protons or electrons. This shows that a significantly larger proportion of photospheric impacts are due to protons compared to electrons. Conversely, a greater proportion of heliospheric crossings are made by electrons compared to protons, although in the $t = 240$ snapshot, the numbers of protons and electrons are nearly equal. Note that while this appears to show a very high ejection rate, this is a reflection of the current sheet biased initialization

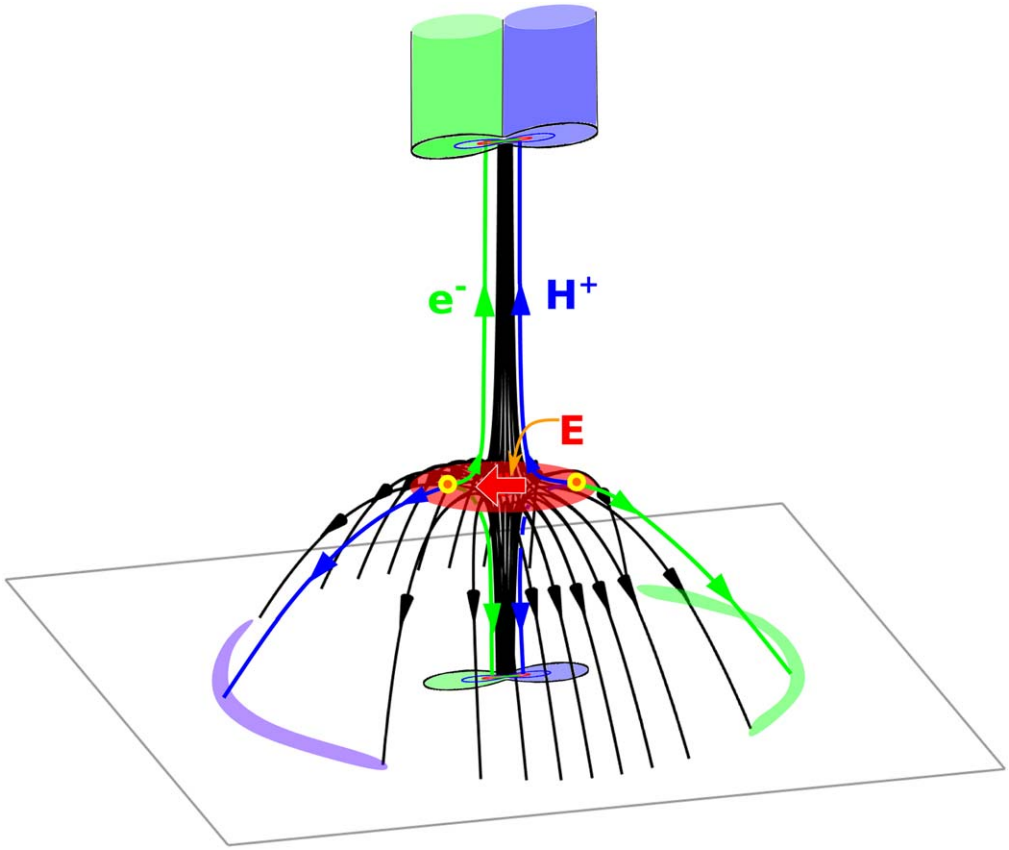

Figure 7. Cartoon demonstrating the mechanism for formation of parallel, spatially separated ion (blue) and electron (green) beams. Particles in the current sheet (red) at positions marked by orange/yellow circles are accelerated either toward or away from the null, depending upon their charge, and are deflected up or down the spine. Color contours on the lower and upper boundaries outline the distribution of Q (based on the analysis of Pontin et al. 2016), which indicates where field lines that pass close to the null are found.

and is not representative of a more evenly distributed population across the entire domain (see Section 3.2 for a brief discussion of the initialized distribution relative to the MHD seeded number density).

We examine now the overall energy spectrum of the accelerated particles. Figure 8 shows the kinetic energy probability distribution functions (PDFs) for all particles crossing the photospheric (blue curve) and heliospheric (green curve) planes, summed over all snapshots. The proton and electron distributions are found to be extremely similar for each of the heliospheric and photospheric incident populations and are therefore combined for readability. Comparing with the initial energy distribution (gold curve), we see that both populations are greatly accelerated to relativistic energies. For both particle species, the kinetic energy PDFs reach maximum energies of order 10 MeV at $t = 220$ and 100 MeV at $t = 240$ and $t = 260$. However, we note that these values are model dependent and that for instance varying the resistivity in the MHD simulation would be expected to result in different final kinetic energies.

A high-energy tail is slightly more apparent in later snapshots, suggesting that there is a greater proportion of nonthermal particles as the fields evolve and larger current sheet structures form. Examining separately the spectra for the photosphere and the heliosphere (not shown), we find that this high-energy tail is most distinct in the heliospheric PDF at $t = 260$. The heliospheric PDFs consistently have a larger number of relatively low-energy particles, although this may be an effect of the selected value of x for the heliospheric plane: lower-energy particles ejected along the jet spire would simply fail to cross the chosen plane during the chosen run time if it were placed further out in the x-direction.

Table 1
Percentage of Total Simulated Population per Snapshot Incident on the Photospheric and Heliospheric Boundaries

	Photosphere		Heliosphere	
Snapshot	Protons	Electrons	Protons	Electrons
$t = 220$	17.7%	5.3%	6.8%	12.9%
$t = 240$	13.6%	6.8%	12.3%	13.9%
$t = 260$	13.5%	5.4%	9.0%	14.2%

There are two possible reasons for this increase in maximum particle energy as the field geometry evolves: either the largest values of $|J|/|B|$ in the current sheet are consistently higher or the volume of the current layer is increasing, so that particles are accelerated over a greater distance. Analyzing $|J|/|B|$ for all three snapshots indicated that the maximum values of $|J|/|B|$ are not changing significantly as the field evolves. Examining the physical size of the current surface (shown in Figure 1) reveals that the surface gets significantly larger as the field evolves, indicating that this is likely the principal source of the increase in maximum particle energy in later snapshots.

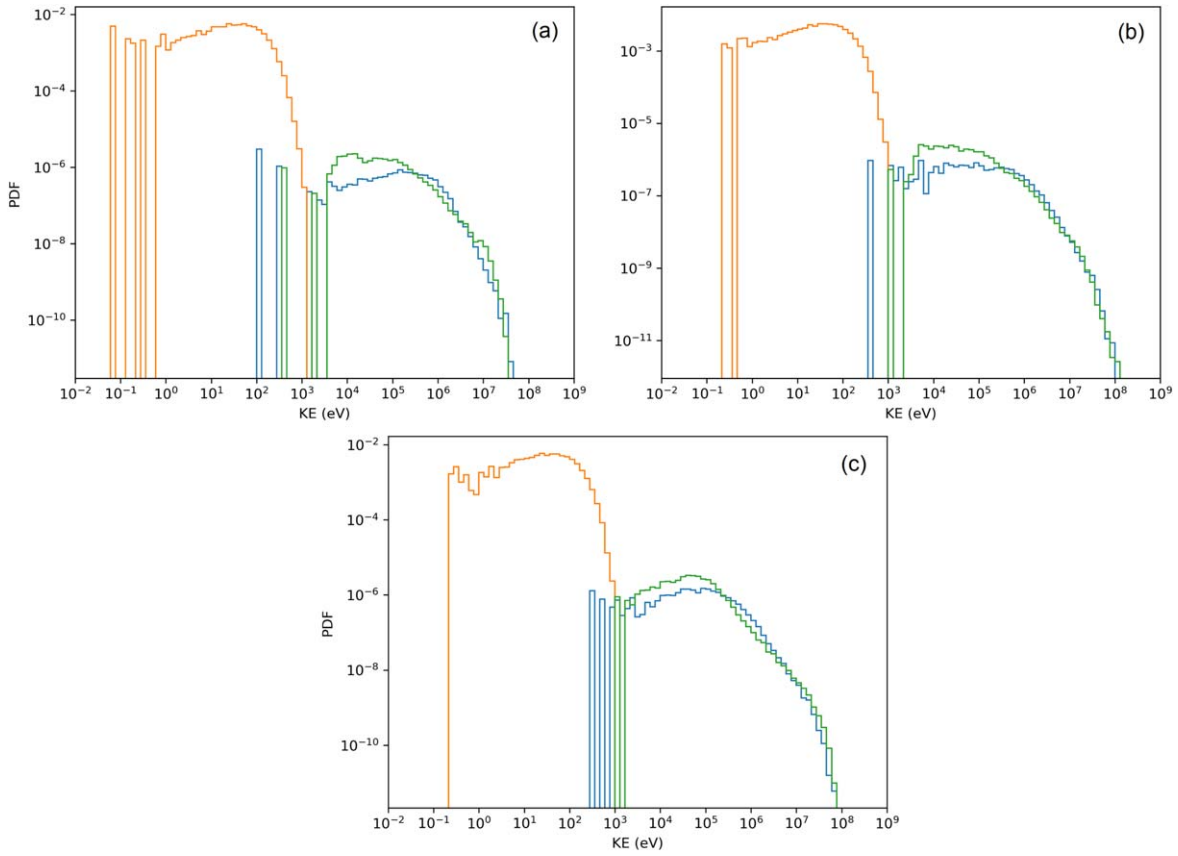

Figure 8. Probability distribution function (PDF) of initial kinetic energies (orange) and incident kinetic energies at photospheric boundary $x = +0.01$ (blue) and heliospheric boundary $x = +60.0$ (green) for (a) $t = 220$, (b) $t = 240$, and (c) $t = 260$.

5. Conclusions

We have calculated the acceleration of test particles, protons and electrons, within a numerical simulation of a solar coronal jet. The kinetic energy distributions of particles incident on the photosphere and ejected into the heliosphere consist of Maxwellians with high-energy, nonthermal tails for both species. The populations reach a maximum kinetic energy of order 100 MeV at $t = 240$ and $t = 260$, increasing slightly from the maximum energies 20–50 MeV at $t = 220$. In all simulated snapshots, the highest-energy particles adhered to the spine and fan plane of the dome structure, which we identified via maps of the squashing factor Q on the boundaries. The accelerated particles were ejected both downwards toward the photospheric boundary upon which they impacted and upwards along the jet spire into the outer corona and heliosphere.

Our results have important implications for interpreting two principal types of observations. Jets such as those that we have modeled are ubiquitously seen in open-field regions on the Sun. In such regions, particles incident on the upper boundary of our simulation domain would stream out into the heliosphere. This outgoing jet of high-energy particles rotates around the overall jet axis. Both protons and electrons are closely aligned to the topological structures in the magnetic field (null-point spine and fan structures), but critically are not coaligned. Therefore, a key prediction of our model is the propagation of adjacent, but not significantly overlapping, proton and electron beams in the heliosphere. These may be detectable through in situ measurements by, for example, the PSP.

Particles accelerated toward the lower boundary of our domain would impact high-density lower layers of the atmosphere, leading to emission in chromospheric and photospheric lines. Figures 3 and 4 clearly predict the formation of circular ribbons at the base of the coronal jet, consistent with observations of quasi-circular EUV emission in on-disk coronal jets (Panesar et al. 2016; Kumar et al. 2019), similar in nature to circular flare ribbons in much larger coronal mass ejections (Ugarte-Urra et al. 2007; Masson et al. 2009; Wang & Liu 2012; Deng et al. 2013; Liu et al. 2015; Shen et al. 2019). Also present in observations is a bright point source, often called a kernel, in the center of the circular ribbon. The source becomes elongated as the flare progresses, due to the asymmetry of the null-point geometry (Pontin et al. 2016). This feature is also produced in our simulations, and indeed it is where the highest particle energy deposition per unit area occurs (see Figure 4). This finding is consistent with the results of Jardins et al. (2009), who found that the positions and motions of some HXR footpoints are correlated with the photospheric intersections of spine field lines.

Other key observational features of flare ribbons include the motion of bright, often spiral, features along the flare ribbons as they separate. There can be more than two HXR footpoints during a flare (Fletcher & Hudson 2002; Lin et al. 2003; Temmer et al. 2007) that are observed to move parallel or antiparallel to the magnetic polarity inversion line and flare ribbons (Fletcher & Hudson 2002; Qiu et al. 2002; Miklenic et al. 2007). Li & Zhang (2015) and Brannon et al. (2015) observed the motion of bright knots within flare ribbons in concert with quasi-periodic slipping of flare loops. One proposed explanation for all of these motions is bursty dynamics in the flare current layer. The flux ropes formed

during tearing of the flare current layer lead to spiral magnetic field structures (Wyper & Pontin 2014b; Pontin & Wyper 2015; Wyper et al. 2016). Pallister et al. (2019) found that the highest-energy particles are closely aligned with these flux ropes. Similar to these previous studies, in our simulations we find that flux ropes form as the current layer becomes unstable, leading to corrugation of the boundary between open and closed flux. The particle impacts follow these corrugations, with concave, hook-like structures forming at the base of the flux ropes. The simulated nonthermal particles with the highest kinetic energies impact the surface at these concave features. The relation between the current-layer dynamics and the particle deposition should be further studied using a time-dependent analysis, in order to understand the link between the two. Such an analysis also would reveal the extent to which the motions on the photosphere are enabled by the current-layer dynamics, which are not directly observable.

As discussed in Section 3 there are effects not modeled in our test-particle method that would have affected our results and how we interpret them. The inclusion of scattering would reduce the kinetic energy of the highest-energy particles, resulting in lower energies on the impact maps and in the tail of the kinetic energy distributions of the ejecta. Additionally, the pitch-angle diffusion due to scattering would lead to fewer particles so closely aligned to separatrices in the impact maps, producing more diffuse impact patterns. In this paper we have used a simple collision-free test-particle approach, but in future studies this could be extended in various ways to provide more realistic particle trajectories. For example, particle scattering could be included, as has previously been implemented for guiding-center test-particle simulations by Borissov et al. (2017, 2020).

Furthermore, as already mentioned, a natural extension to this work would be to consider acceleration in time-dependent fields, which would include the effects of additional acceleration mechanisms. For example, simulations performed by le Roux et al. (2015, 2018) and by Zhou et al. (2018) showed that particles in evolving flux ropes are accelerated over time as the ropes contract and the particles undergo multiple magnetic reflections. Simulations of both the initial guiding and subsequent acceleration of flux-rope adjacent particles would give a more complete picture of how flux ropes affect the overall motion of particles. It would also alleviate the current issue where simulated proton run times are longer than the Alfvén travel time. In addition, future work could also address the role of different resistivity models and values on the MHD evolution of the jet and its effect on particle energies and trajectories. Finally, to obtain a more detailed and quantitative picture of particle acceleration in a jet, a kinetic or particle-in-cell (PIC) model for coronal particle acceleration could be applied to this jet geometry with which to compare the test-particle approach. There are existing kinetic and PIC studies in MHD-generated jets similar to the one examined in this study (Baumann & Nordlund 2012, Baumann et al. 2013) that demonstrate nonthermal acceleration and photospheric impact distributions. Alternatively, in future a hybrid fluid-kinetic simulation approach could be employed (see, e.g., the recent work of Drake et al. 2019, Arnold et al. 2021, or Marcowith et al. 2020 for a review of different methods). Such methods are capable of investigating the formation of electric fields due to charge separation and how they may affect subsequent particle acceleration. We note that with present computational resources it is already a substantial calculation in MHD to include the full jet geometry and sufficiently resolve the reconnection site to observe current sheet fragmentation as in the present study.

The authors thank James Threlfall and Thomas Neukirch for assistance in adapting `party_orb` for use in tandem with our code. We would also like to thank Simon Cadelaresi for providing us with the field-line integration code as well as assistance in its use. R.P. acknowledges studentship funding from STFC through grant ST/N504026. D.P. was supported by STFC under grants ST/N000714 and ST/S000267. C.R.D. was supported by NASA's H-ISFM program. This work used the DiRAC Data Analytic system at the University of Cambridge, operated by the University of Cambridge High Performance Computing Service on behalf of the STFC DiRAC HPC Facility (www.dirac.ac.uk). This equipment was funded by BIS National E-infrastructure capital grant (ST/K001590/1), STFC capital grants ST/H008861/1 and ST/H00887X/1, and STFC DiRAC Operations grant ST/K00333X/1. DiRAC is part of the National E-Infrastructure.

Appendix A
Full-motion Adams Method

The predictor-corrector method used is an Adams method, composed of an Adams–Bashforth predictor (an explicit method) and an Adams–Moulton corrector (an implicit method). Equation (A1) is a general expression for the Adams–Bashforth predictor (Antia 2002). This uses n past data (uniformly spaced by time step h) for the time derivative of a general variable f to predict a value f_p one time step h later. This value f_p is then used to predict the value of the time derivative of f one time step later (df^p_{i+1}/dt). Equation (A2) shows the Adams–Moulton corrector, which uses this to calculate the corrected value of f one time step later (f_{i+1}).

$$f_p = f_i + \frac{h}{K}\left(a_{i-n}\frac{df_{i-n}}{dt} + a_{i-n+1}\frac{df_{i-n+1}}{dt} + \ldots + a_i\frac{df_i}{dt}\right), \tag{A1}$$

$$f_{i+1} = f_i + \frac{h}{K}\left(b_{i-n+1}\frac{df_{i-n+1}}{dt} + b_{i-n+2}\frac{df_{i-2+1}}{dt} + \ldots + b_{i+1}\frac{df^p_{i+1}}{dt}\right), \tag{A2}$$

where K, a, and b are coefficients. The values of the coefficients, obtained using polynomial interpolation, depend upon the order of the method used; a and b are specific to the predictor and corrector algorithms, respectively.

A sixth-order combined Adams method (Mathews & Fink 1998) to solve a position value with relativistic momenta is shown in Equations (A3)–(A6)

$$\boldsymbol{r}_p = \boldsymbol{r}_0 + \frac{1}{m_0}\frac{h}{1440}\left(-475\frac{\boldsymbol{p}_{-5}}{\gamma_{-5}} + 2877\frac{\boldsymbol{p}_{-4}}{\gamma_{-4}} - 7298\frac{\boldsymbol{p}_{-3}}{\gamma_{-3}} + 9982\frac{\boldsymbol{p}_{-2}}{\gamma_{-2}} - 7923\frac{\boldsymbol{p}_{-1}}{\gamma_{-1}} + 4277\frac{\boldsymbol{p}_0}{\gamma_0}\right), \tag{A3}$$

$$\boldsymbol{r}_{+1} = \boldsymbol{r}_0 + \frac{1}{m_0}\frac{h}{1440}\left(27\frac{\boldsymbol{p}_{-4}}{\gamma_{-4}} - 173\frac{\boldsymbol{p}_{-3}}{\gamma_{-3}} + 482\frac{\boldsymbol{p}_{-2}}{\gamma_{-2}} - 798\frac{\boldsymbol{p}_{-1}}{\gamma_{-1}} + 1427\frac{\boldsymbol{p}_0}{\gamma_0} + 475\frac{\boldsymbol{p}_{+1}}{\gamma_{+1}}\right), \tag{A4}$$

$$\boldsymbol{p}_p = \boldsymbol{p}_0 + \frac{h}{1440}\left(-475\frac{d\boldsymbol{p}_{-5}}{dt} + 2877\frac{d\boldsymbol{p}_{-4}}{dt} - 7298\frac{d\boldsymbol{p}_{-3}}{dt} + 9982\frac{d\boldsymbol{p}_{-2}}{dt} - 7923\frac{d\boldsymbol{p}_{-1}}{dt} + 4277\frac{d\boldsymbol{p}_0}{dt}\right), \tag{A5}$$

$$\boldsymbol{p}_{+1} = \boldsymbol{p}_0 + \frac{h}{1440}\left(27\frac{d\boldsymbol{p}_{-4}}{dt} - 173\frac{d\boldsymbol{p}_{-3}}{dt} + 482\frac{d\boldsymbol{p}_{-2}}{dt} - 798\frac{d\boldsymbol{p}_{-1}}{dt} + 1427\frac{d\boldsymbol{p}_0}{dt} + 475\frac{d\boldsymbol{p}^p_{+1}}{dt}\right). \tag{A6}$$

When the predicted position $\boldsymbol{r}_p$ is calculated from Equation (A3), the field values are evaluated at this position and used along with the predicted momentum $\boldsymbol{p}_p$ from Equation (A5) to predict a value for $d\boldsymbol{p}^p_{+1}/dt$ using Equations (10) and (A2). All of the data needed to calculate the corrected solutions $\boldsymbol{r}_p$ and $\boldsymbol{p}_p$ are then available.

Appendix B
Guiding-center Runge–Kutta Method

The guiding-center algorithm is based on the party_orb code developed at the University of St Andrews. The party_orb code solves the field-static relativistic guiding-center with a fourth-order Runge–Kutta scheme. This is a single-step method (Cheney & Kincaid 2007) that solves an equation f as follows:

$$x(t+h) = x(t) + \frac{h}{6}(F_1 + 2F_2 + 2F_3 + F_4), \tag{B1}$$

where

$$F_1 = f(t, x), \tag{B2}$$

$$F_2 = f\left(t + \frac{h}{2}, x + \frac{1}{2}F_1\right), \tag{B3}$$

$$F_3 = f\left(t + \frac{h}{2}, x + \frac{1}{2}F_2\right), \tag{B4}$$

$$F_4 = f(t + h, x + F_3). \tag{B5}$$

Rather than using the party_orb code in its entirety, key sections were selected and adapted into subroutines to work in tandem with the full-motion code. The most recent version of the party_orb code (as of the time of writing) is a relativistic modification of the code used by Giuliani et al. (2005). The code consists of core program files defining the global variables and simulation setup, and separate module files containing: subroutines for importing MHD-generated field values from LaRe3D or creating an analytical field geometry; subroutines for the Runge–Kutta algorithm; and subroutines for solving the relativistic and nonrelativistic guiding-center equations of motion.

Specifically, the modules containing the fourth-order Runge–Kutta algorithm and the evaluation of the relativistic guiding-center equations were selected and adapted for our use. As code to import and scale the MHD-generated fields for the full-motion code had already been developed, party_orb's field-setup subroutines were not needed. Any editing was restricted to the scaling factors, universal constants that are not defined in the selected code sections, and variable names for consistency with the full-motion code and simpler debugging. Additionally party_orb is written in Fortran 90, so some syntax was changed such that the subroutines could be compiled and run as Fortran 95 code, consistent with the full-motion components. The core algorithms for the Runge–Kutta method and the guiding-center equation solutions remain unchanged. While the original party_orb code has been tested and utilized frequently since its creation, the described implementation of it has not. Therefore, new tests were performed to ensure that it was accurate for the intended simulations.

Appendix C
Switching Algorithm

For the guiding-center approximation to be valid, two main assumptions are made. First, the local parallel electric field must be significantly smaller than the local perpendicular electric field. Second, the length scale of the local magnetic field gradient must be significantly larger than the particle's gyroradius. The first of these assumptions fails for particles accelerated by strong parallel electric fields in current sheets. The second assumption fails in regions where the magnetic field gradient is large, such as near magnetic null points. Current sheet structures at sheared, collapsed null points are examples of field geometries where both of these conditions fail.

Instead of relying solely on either the full-motion or guiding-center methods, we developed a method that would switch between them according to whether the properties of the local fields satisfied the assumptions required by the guiding-center approximation. In regions where they are not satisfied, full motion is used to maintain accuracy. In areas where the assumptions are satisfied, the guiding-center approximation is used to simulate the trajectory quickly.

The first main condition for switching is when the gradient scale of the $\boldsymbol{B}$ field is comparable to the Larmor radius of the particle. If the $\boldsymbol{B}$ field changes significantly across an orbit, one cannot assume that the particle undergoes symmetric gyromotion. As such, we calculate the length scale of the spatial field derivative,

$$L_B \equiv \frac{B}{|\nabla B|}. \tag{C1}$$

We take the ratio of this length to the Larmor radius r_L and compare the result to a manually chosen threshold $L_{B_{\rm th}}$, switching from guiding-center to full-motion when it exceeds this value.

$$\text{If} \quad \frac{L_B}{r_L} \geqslant L_{B_{\rm th}}, \quad \text{switch from GC to FM.} \tag{C2}$$

The second main condition depends on the $\boldsymbol{E}$ field component parallel to $\boldsymbol{B}$. The derivation of the guiding-center approximation (Northrop 1961) requires that the component of $\boldsymbol{E}$ parallel to $\boldsymbol{B}$, $\boldsymbol{E}_{||}$, be of an order that is negligible compared to the perpendicular component, $\boldsymbol{E}_{\perp}$. This is quantified by calculating the ratio of the magnitudes and comparing the result

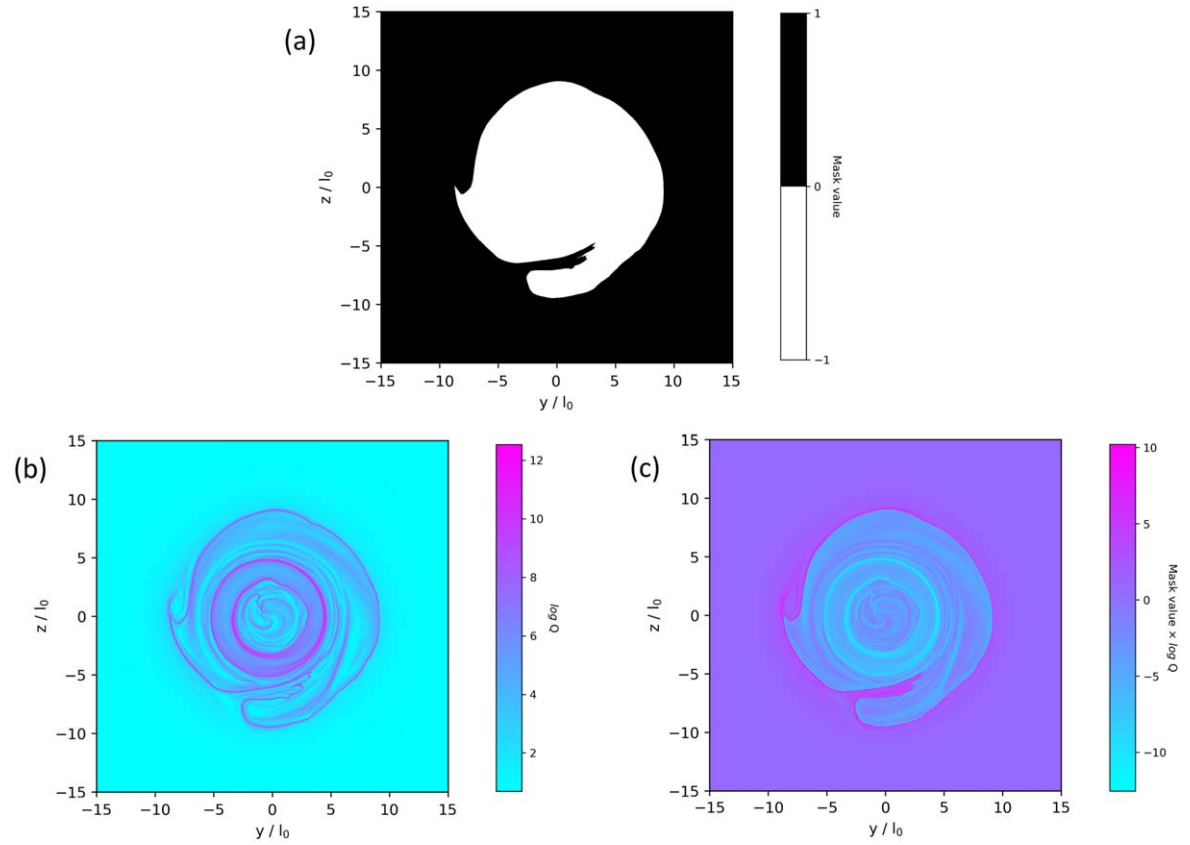

Figure 9. Connectivity Q maps at the photospheric boundary for the snapshot $t = 4$, where (a) shows the binary mask to be applied to the log Q map by multiplication, (b) shows the log Q map without any modification, and (c) shows the final map of the masked log Q values at the photosphere.

to another user-selected threshold value EF_{th}.

$$\text{If} \quad \frac{E_{||}}{|\boldsymbol{E}_{\perp}|} \geqslant EF_{\text{th}}, \quad \text{switch from GC to FM.} \tag{C3}$$

Switching from full-motion to guiding-center involves converting the 3D position vector and 3D momentum vector of a particle into a 3D position vector of the particle gyrocenter, the magnitude of the particle velocity parallel to the local magnetic field vector, and the magnitude of the magnetic moment of the particle. These values are calculated with the following equations:

$$\begin{aligned}
\boldsymbol{R} &= \boldsymbol{r} + \frac{m}{q}\frac{1}{B}\gamma\left[\left(\frac{\boldsymbol{p}}{m} - \boldsymbol{v}_E\right) \times \hat{\boldsymbol{B}}\right],\\
\boldsymbol{v}_E &= \frac{\boldsymbol{E} \times \boldsymbol{B}}{B^2},\\
U_{||} &= \gamma(\boldsymbol{v} \cdot \hat{\boldsymbol{B}}),\\
\boldsymbol{v}_{\perp} &= \boldsymbol{v} - \frac{U_{||} \cdot \hat{\boldsymbol{B}}}{\gamma} - \boldsymbol{v}_E,\\
\mu_r &= \frac{m\gamma^2 \boldsymbol{v}_{\perp}^2}{2B}.
\end{aligned} \tag{C4}$$

Switching from guiding-center to full-motion is more complicated, as it involves converting five values into six values. The guiding-center method does not track the position of the particle about its orbit; hence a random phase angle θ of the full orbit between 0 and 2π is generated when the switch from guiding-center to full-motion occurs. The values for full-motion are then calculated with the following equations:

$$\begin{aligned}
\boldsymbol{r} &= \boldsymbol{R} + r_L(\hat{\boldsymbol{e}}_2 \cos(\theta) - \hat{\boldsymbol{e}}_1 \sin(\theta)),\\
\boldsymbol{p} &= m\gamma U_{||}\hat{\boldsymbol{B}} + (\boldsymbol{e}_1 \cos(\theta) + \boldsymbol{e}_2 \sin(\theta))|\boldsymbol{p}_{\perp}| + \boldsymbol{p}_E.
\end{aligned} \tag{C5}$$

Here, $\boldsymbol{p}_E$ represents all drift terms in the guiding-center approximation, in principle, but as the $\boldsymbol{E} \times \boldsymbol{B}$ drift is assumed to be dominant in field geometries with significant $\boldsymbol{E}$ fields, we assume that all other drift terms are negligible. Terms $\hat{\boldsymbol{e}}_1$ and $\hat{\boldsymbol{e}}_2$ are orthonormal unit vectors given by

$$\begin{aligned}
\boldsymbol{e}_1 &= \frac{\boldsymbol{R} \times \hat{\boldsymbol{B}}}{R},\\
\boldsymbol{e}_2 &= \hat{\boldsymbol{B}} \times \boldsymbol{e}_1.
\end{aligned} \tag{C6}$$

Appendix D
Q Map Masking

At various points in the paper we discuss and plot a masked value of the squashing factor, Q. This is done to encode extra information in the figures: since Q is strictly positive by definition, we can use a signed function to denote open and closed field lines. The masked Q plots are constructed as follows. First, we calculate Q for all field lines that thread the lower boundary (representing the photosphere). Next, we create a "mask" by identifying closed and open field lines. These are defined as field lines that connect back to the lower boundary, or those that connect from the lower boundary to the upper boundary, respectively. The mask takes value $+1$ for an open field line and -1 for a closed field line; see, e.g., Figure 9(a).

To produced the masked Q distribution (Figure 9(c)) we then simply evaluate the product of Q (Figure 9(b)) and the mask (Figure 9(a)).

ORCID iDs

Ross Pallister https://orcid.org/0000-0002-2376-6725
Peter F. Wyper https://orcid.org/0000-0002-6442-7818
David I. Pontin https://orcid.org/0000-0002-1089-9270
C. Richard DeVore https://orcid.org/0000-0002-4668-591X

References

Antia, H. M. 2002, Numerical Methods for Scientists and Engineers (1st ed.; Basel: Birkhauser)
Arnold, H., Drake, J. F., Swisdak, M., et al. 2021, PhRvL, 126, 135101
Bain, H. M., & Fletcher, L. 2009, A&A, 508, 1443
Baumann, G., & Nordlund, Å. 2012, ApJL, 759, L9
Baumann, G., Galsgaard, K., & Nordlund, Å. 2013, SoPh, 284, 467
Baumann, G., Haugbølle, T., & Nordlund, Å. 2013, ApJ, 771, 93
Borissov, A., Kontar, E. P., Threlfall, J., & Neukirch, T. 2017, A&A, 605, A73
Borissov, A., Neukirch, T., Kontar, E. P., Threlfall, J., & Parnell, C. E. 2020, A&A, 635, A63
Brannon, S. R., Longcope, D. W., & Qiu, J. 2015, ApJ, 810, 4
Bučík, R., Innes, D. E., Mason, G. M., et al. 2018, ApJ, 852, 76
Chen, B., Yu, S., Battaglia, M., et al. 2018, ApJ, 866, 62
Cheney, E. W., & Kincaid, D. R. 2007, Numerical Mathematics and Computing (6th ed.; Pacific Grove, CA: Brooks/Cole Publishing)
Chiti, F. 2020, FedericaChiti/Null_Finder: Null Finder—Release 1, v1.0.0, Zenodo, doi:10.5281/zenodo.4308622
Dalla, S., & Browning, P. K. 2005, A&A, 436, 1103
Dalla, S., & Browning, P. K. 2008, A&A, 491, 289
Dalla, S., Marsh, M. S., & Battarbee, M. 2017, ApJ, 834, 167
Dalla, S., Marsh, M. S., & Laitinen, T. 2015, ApJ, 808, 62
De Pontieu, B., Title, A. M., Lemen, J. R., et al. 2014, SoPh, 289, 2733
Deng, N., Tritschler, A., Jing, J., et al. 2013, ApJ, 769, 112
DeVore, C. R., & Antiochos, S. K. 2008, ApJ, 680, 740
Doyle, L., Wyper, P. F., Scullion, E., et al. 2019, ApJ, 887, 246
Drake, J. F., Arnold, H., Swisdak, M., & Dahlin, J. T. 2019, PhPl, 26, 012901
Fletcher, L., & Hudson, H. S. 2002, SoPh, 210, 307
Giuliani, P., Neukirch, T., & Wood, P. 2005, ApJ, 635, 636
Glesener, L., & Fleishman, G. D. 2018, ApJ, 867, 84
Glesener, L., Krucker, S., & Lin, R. P. 2012, ApJ, 754, 9
Grady, K. J., Neukirch, T., & Giuliani, P. 2012, A&A, 546, A85
Haynes, A. L., & Parnell, C. E. 2007, PhPl, 14, 082107
Innes, D. E., Bučík, R., Guo, L. J., & Nitta, N. 2016, AN, 337, 1024
Jardins, A. D., Canfield, R., Longcope, D., Fordyce, C., & Waitukaitis, S. 2009, ApJ, 693, 1628
Ji, H., & Daughton, W. 2011, PhPl, 18, 111207
Karpen, J. T., Antiochos, S. K., & DeVore, C. R. 2012, ApJ, 760, 81
Kress, B. T., Hudson, M. K., Looper, M. D., et al. 2007, JGRA, 112, A09215
Krucker, S., Kontar, E. P., Christe, S., Glesener, L., & Lin, R. P. 2011, ApJ, 742, 82
Krucker, S., Larson, D. E., Lin, R. P., & Thompson, B. J. 1999, ApJ, 519, 864
Kumar, P., Karpen, J. T., Antiochos, S. K., et al. 2019, ApJ, 873, 93
le Roux, J. A., Zank, G. P., & Khabarova, O. V. 2018, ApJ, 864, 158
le Roux, J. A., Zank, G. P., Webb, G. M., & Khabarova, O. 2015, ApJ, 801, 112
Lemen, J. R., Title, A. M., Akin, D. J., et al. 2012, The Atmospheric Imaging Assembly (AIA) on the Solar Dynamics Observatory (SDO) (New York: Springer), 17
Li, H., & Yang, J. 2019, ApJ, 872, 87
Li, T., & Zhang, J. 2015, ApJL, 804, L8
Li, X., Guo, F., & Liu, Y.-H. 2021, PhPl, 28, 052905
Lin, R. P., Krucker, S., Hurford, G. J., et al. 2003, ApJL, 595, L69
Liu, C., Deng, N., Liu, R., et al. 2015, ApJL, 812, L19
Marcowith, A., Ferrand, G., Grech, M., et al. 2020, LRCA, 6, 1
Masson, S., Pariat, E., Aulanier, G., & Schrijver, C. J. 2009, ApJ, 700, 559
Masson, S., Pariat, E., Valori, G., et al. 2017, A&A, 604, A76
Mathews, J. H., & Fink, K. D. 1998, Numerical Methods Using MATLAB (3rd ed.; New York: Simon & Schuster)
Miklenic, C. H., Veronig, A. M., Vrsnak, B., & Hanslmeier, A. 2007, A&A, 461, 697
Moore, T. E., Fok, M.-C., Delcourt, D. C., Slinker, S. P., & Fedder, J. A. 2010, JGRA, 115, A00J14
Mulay, S. M., Tripathi, D., Del Zanna, G., & Mason, H. 2016, A&A, 589, A79
Musset, S., Jeunon, M., & Glesener, L. 2020, ApJ, 889, 183
Nitta, N. V., Mason, G. M., Wang, L., Cohen, C. M. S., & Wiedenbeck, M. E. 2015, ApJ, 806, 235
Northrop, T. G. 1961, AnPhy, 15, 79
Northrop, T. G. 1963, RvGeo, 1, 283
Pallister, R., Pontin, D. I., & Wyper, P. F. 2019, A&A, 622, A207
Panesar, N. K., Sterling, A. C., Moore, R. L., & Chakrapani, P. 2016, ApJL, 832, L7
Pariat, E., Antiochos, S. K., & DeVore, C. R. 2009, ApJ, 691, 61
Platten, S. J., Parnell, C. E., Haynes, A. L., Priest, E. R., & Mackay, D. H. 2014, A&A, 565, A44
Pontin, D., Galsgaard, K., & Démoulin, P. 2016, SoPh, 291, 1739
Pontin, D. I., Bhattacharjee, A., & Galsgaard, K. 2007, PhPl, 14, 052106
Pontin, D. I., & Wyper, P. F. 2015, ApJ, 805, 39
Priest, E. R., & Pontin, D. I. 2009, PhPl, 16, 122101
Qiu, J., Lee, J., Gary, D. E., & Wang, H. 2002, ApJ, 565, 1335
Rachmeler, L. A., Pariat, E., DeForest, C. E., Antiochos, S., & Török, T. 2010, ApJ, 715, 1556
Raouafi, N. E., Patsourakos, S., Pariat, E., et al. 2016, SSRv, 201, 1
Rosdahl, K. J., & Galsgaard, K. 2010, A&A, 511, A73
Savcheva, A., Cirtain, J., Deluca, E. E., et al. 2007, PASJ, 59, S771
Shen, Y. 2021, RSPSA, 477, 20200217
Shen, Y., Qu, Z., Zhou, C., et al. 2019, ApJL, 885, L11
Stanier, A., Browning, P., & Dalla, S. 2012, A&A, 542, A47
Sterling, A. C., Moore, R. L., Falconer, D. A., & Adams, M. 2015, Natur, 523, 437
Temmer, M., Veronig, A. M., Vršnak, B., & Miklenic, C. 2007, ApJ, 654, 665
Threlfall, J., Neukirch, T., Parnell, C. E., & Eradat Oskoui, S. 2015, A&A, 574, A7
Threlfall, J., Stevenson, J. E. H., Parnell, C. E., & Neukirch, T. 2016, A&A, 585, A95
Titov, V. S., Mikić, Z., Linker, J. A., Lionello, R., & Antiochos, S. K. 2011, ApJ, 731, 111
Titov, V. S., Tassi, E., & Hornig, G. 2004, PhPl, 11, 4662
Ugarte-Urra, I., Warren, H. P., & Winebarger, A. R. 2007, ApJ, 662, 1293
Wang, H., & Liu, C. 2012, ApJ, 760, 101
Wiedenbeck, M. E., Bučík, R., Mason, G. M., et al. 2020, ApJS, 246, 42
Wood, P., & Neukirch, T. 2005, SoPh, 226, 73
Wyper, P. F., & DeVore, C. R. 2016, ApJ, 820, 77
Wyper, P. F., DeVore, C. R., & Antiochos, S. K. 2019, MNRAS, 490, 3679
Wyper, P. F., DeVore, C. R., Karpen, J. T., & Lynch, B. J. 2016, ApJ, 827, 4
Wyper, P. F., & Pontin, D. I. 2014a, PhPl, 21, 082114
Wyper, P. F., & Pontin, D. I. 2014b, PhPl, 21, 102102
Zharkova, V. V., Arzner, K., Benz, A. O., et al. 2011, SSRv, 159, 357
Zhou, M., El-Alaoui, M., Lapenta, G., et al. 2018, JGRA, 123, 8087